



Upper limb joint forces and moments during underwater cyclical movements



Jessy Lauer^{a,b,*}, Annie Hélène Rouard^b, João Paulo Vilas-Boas^a

^a Center of Research, Education, Innovation and Intervention in Sport, Faculty of Sport, and Porto Biomechanics Laboratory, University of Porto, Portugal

^b Inter-university Laboratory of Human Movement Biology, University Savoie Mont Blanc, Le Bourget du Lac, France

ARTICLE INFO

Article history:

Accepted 20 August 2016

Keywords:

Joint load
Inverse dynamics
Computational fluid dynamics
Aquatic exercise

ABSTRACT

Sound inverse dynamics modeling is lacking in aquatic locomotion research because of the difficulty in measuring hydrodynamic forces in dynamic conditions. Here we report the successful implementation and validation of an innovative methodology crossing new computational fluid dynamics and inverse dynamics techniques to quantify upper limb joint forces and moments while moving in water. Upper limb kinematics of seven male swimmers sculling while ballasted with 4 kg was recorded through underwater motion capture. Together with body scans, segment inertial properties, and hydrodynamic resistances computed from a unique dynamic mesh algorithm capable to handle large body deformations, these data were fed into an inverse dynamics model to solve for joint kinetics. Simulation validity was assessed by comparing the impulse produced by the arms, calculated by integrating vertical forces over a stroke period, to the net theoretical impulse of buoyancy and ballast forces. A resulting gap of $1.2 \pm 3.5\%$ provided confidence in the results. Upper limb joint load was within 5% of swimmer's body weight, which tends to supports the use of low-load aquatic exercises to reduce joint stress. We expect this significant methodological improvement to pave the way towards deeper insights into the mechanics of aquatic movement and the establishment of practice guidelines in rehabilitation, fitness or swimming performance.

© 2016 Elsevier Ltd. All rights reserved.

1. Introduction

Inverse dynamics provides kinetic quantities such as net joint moments, compressive and shear joint forces, or power flow across segments, from differentiated kinematics and external forces acting upon the body (Hatze, 2002). This approach has proved crucial to answer fundamental questions common to biomechanics and physiology, unveiling, among others, the mechanical determinants of overground locomotion metabolic cost and efficiency (Sawicki and Ferris, 2009, 2008), how joints modulate net power output (Farris and Sawicki, 2012; Roberts and Belliveau, 2005), how muscles work (Winter, 1983), strategies to reduce joint loading in the prevention and treatment of running-related injuries (Heiderscheit et al., 2011), or the mechanical bases to design biomimetic prostheses (Collins et al., 2015; Hansen et al., 2004).

These key questions have received considerable attention in terrestrial locomotion; yet, they remain unanswered in water-based activities, impeding our understanding of human aquatic

'performance'. Unlike on land where external forces are easily measured via force platforms, they are very hard to estimate in water. The prediction of fluid forces on a swimmer's hand has been achieved through pressure measurements (Kudo et al., 2008), sensors however only provide pressure at specific hand locations and thus do not offer a complete hydrodynamics picture, nor do they precisely reflect the actual instantaneous point of force application. Furthermore, external forces at the hand are insufficient to solve the inverse dynamics problem, and those at the forearm and upper arm are simultaneously needed. This method is therefore poorly suited to inverse dynamics modeling. The strip theory approach, which is a different one that consists in partitioning a system made of geometrical shapes into many thin strips on which fluid forces are computed, has also been carried out (Biscarini and Cerulli, 2007; Orselli and Duarte, 2011), though lift was ignored and the analysis was restricted to the lower limb in the sagittal plane. In the case of 3D motions, or upper limb movements where lift likely takes a more prominent place as forces are generated from cambered body surfaces (Takagi et al., 2013), such an approach would introduce complicated mathematical expressions to account for all forces acting on the moving segments and, thus, is not satisfactory for the purpose of estimating the joint load.

* Correspondence to: LIBM, Bâtiment Les Belledonnes, 73376 Le Bourget du Lac cedex, France.

E-mail address: jessy.lauer@gmail.com (J. Lauer).

Over the last decade, the use of computational fluid dynamics (CFD) has emerged in aquatic locomotion research as a promising alternative to those issues. It has the advantage of providing enhanced hydrodynamic force calculations, yet mostly limited to the investigation of swimmer's gliding positions (Costa et al., 2015; Zaïdi et al., 2008) or rigid arm models in various configurations (Marinho et al., 2011; Rouboa et al., 2006). Rouboa et al. (2006) recognized the difficulty in prescribing true kinematics with acceleration/deceleration, multi-axial rotations, limb deformation at the joints, and mesh motion. This is because commercial CFD software solutions lack features to deal with complex 3D deformations, which in turn does not allow the quantification of resistive forces acting upon a whole limb in dynamic conditions. As of today, this problem poses one of the major challenge of aquatic movement research (Biscarini and Cerulli, 2007), and by extension, hydrotherapy, competitive swimming, and aquatic fitness.

In view of the above-mentioned issues, we developed two innovative integrated techniques to assess upper limb joint load in water: a dynamic mesh CFD algorithm to smoothly handle large body deformations and compute instantaneous hydrodynamic forces at the hand, forearm and upper arm in dynamic conditions, coupled with an inverse dynamics model specifically designed for complex joints. We first tested the methodological hypothesis that CFD, when integrated with inverse dynamics, could reliably be used to assess upper limb joint load in water. Second, given the growing popularity of aquatic therapy but the lack of mechanical evidence for its benefits, we computed upper limb joint forces and moments to check whether joint load would be low and supportive of the implementation of upper limb aquatic exercises for rehabilitation.

2. Material and methods

2.1. Kinematic data collection and pre-processing

Seven experienced, right-handed male swimmers (25.3 ± 2.6 years, 1.80 ± 0.06 m, 73.5 ± 6.8 kg) provided written informed consent to participate in the study. Approval for all experimental procedures was granted by the University of Porto ethics committee. Participants were sculling at the middle of a 25-m long, 2-m deep indoor swimming pool, while ballasted with 4 kg (effective underwater weight: 34 N) tied at the waist. They were instructed to remain stationary head above the water surface for about 10 s. Such an ∞ -shaped sculling motion (divided into down and upstroke; see Fig. 1) was chosen since it naturally incorporates flow phenomena that are responsible for high force production in regular competitive strokes (Takagi et al., 2014), and is an exercise frequently used in fitness and rehabilitation programs.

3D kinematics data were captured in the inertial coordinate system (ICS) by automatically tracking 12 reflective markers positioned along the right upper limb and thorax (see Fig. 2) using a 12-camera underwater motion capture setup (Qualisys, Gothenburg, Sweden). Ten cameras were mounted along two opposite sides of the pool, just below the water surface, and the two others at the bottom of the pool facing upwards. A volume of approximately 9 m^3 (3 m long, 2 m wide, 1.5 m deep) was calibrated using an L-shaped reference structure and moving a wand with two markers (inter-point distance: 0.7495 m) according to manufacturer's recommendations. Marker reconstruction accuracy reached 99.8%.

Of the 10 s of data collection, we retained for processing four sculling strokes per subject satisfying the task instruction to move as little as possible, selected on the basis of the stability of xiphoid process marker vertical displacement. Markers trajectories were low-pass filtered (4th order Butterworth filter, cutoff frequency of 6 Hz). Segment coordinate systems (SCS; thorax, upper arm, forearm and hand) were constructed according to the right-hand rule with the X-axis directed anteriorly (abduction/adduction axis), the Y-axis superiorly (internal/external rotation axis) and the Z-axis laterally to the right (flexion/extension axis), and embedded respectively at the suprasternal notch, glenohumeral joint center (estimated from the calculation diagram provided by Reed et al. (1999)), ulnar styloid and third metacarpal (Table 1 and Fig. 2). Joint angle time series—later on required into the dynamic mesh algorithm to realistically deform the body—were computed from the relative motion between two adjacent SCS through the Z–X–Y Euler angles sequence. These procedures agreed with the International Society of Biomechanics

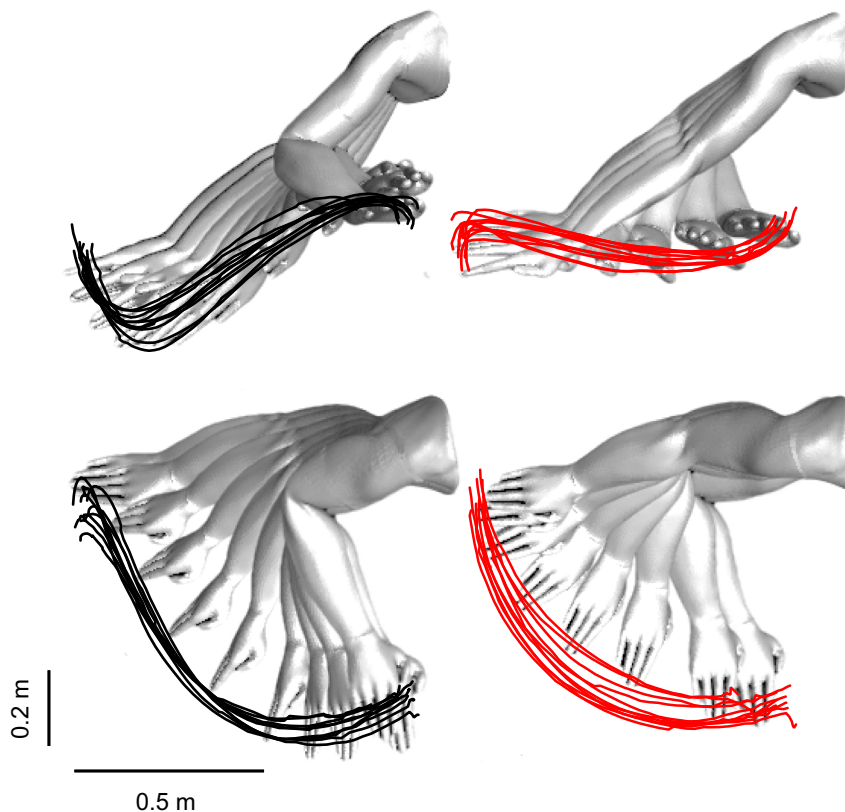


Fig. 1. Middle finger tip trajectories in the frontal (top) and transverse (bottom) planes captured from Qualisys cameras superimposed on the upper limb geometry numerically deformed every 0.05 s (19 frames). Black traces are downstroke (when the arms are horizontally adducted); red traces, upstroke (when the arms are horizontally abducted after stroke reversal). Note how virtual upper limb motion matches experimental kinematics. (For interpretation of the references to color in this figure legend, the reader is referred to the web version of this article.)

(ISB) convention (Wu et al., 2005), and were carried out in MATLAB® R2014a (The MathWorks, Inc., Natick, MA, USA).

2.2. Numerical method

Body geometries were obtained from a Mephisto 3D scanner (4DDynamics, Antwerp, Belgium), further edited and converted into a 3D computer-aided design model prior to import into ANSYS® Fluent® Release 14.5 software (ANSYS, Inc., Canonsburg, PA, USA). The computational domain was a cube of 3-m edges, single phase with no air-water interface, and discretized into unstructured tetrahedral cells. Domain size independence was checked with domain boundaries gradually moved further away from the geometry until no change in hydrodynamic forces occurs to guarantee that the results are not affected. A virtual rectangular body of

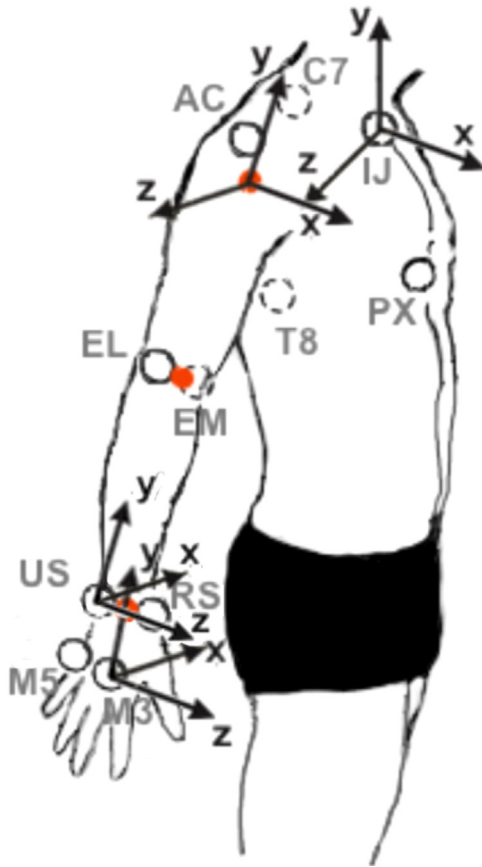


Fig. 2. Right upper limb kinematic model. Markers are shown as open circles and joint centers as red dots. Right-handed segment coordinate systems follow ISB recommendations (Wu et al., 2005), the X-, Y- and Z-axes respectively pointing anteriorly, superiorly and laterally to the right. PX: xiphoid process; LJ: suprasternal notch; C7: spinous process at C7; T8: spinous process at T8; AC: acromion process; EL: lateral epicondyle; EM: medial epicondyle; US: ulnar styloid; RS: radial styloid; M3: third metacarpal; M5: fifth metacarpal; and an additional piece of reflective tape at the tip of the middle finger (not represented here). (For interpretation of the references to color in this figure legend, the reader is referred to the web version of this article.)

Table 1

Definitions of the segment coordinate systems for the right-hand side. $\overline{m}_{\text{SUBSCRIPT}}$ stands for marker locations, and \overline{gh} , the glenohumeral joint center location estimated as in Reed et al. (1999).

Segment	X-axis	Y-axis	Z-axis
Thorax	$\overline{t}_x = \overline{t}_y \times \overline{t}_z$	$\overline{t}_y = \frac{(\overline{m}_{lj} + \overline{m}_{c7})/2 - (\overline{m}_{px} + \overline{m}_{t8})/2}{ \overline{m}_{lj} - \overline{m}_{c7} \times \overline{t}_y}$	$\overline{t}_z = \frac{\overline{m}_{lj} - \overline{m}_{c7}}{ \overline{m}_{lj} - \overline{m}_{c7} \times \overline{t}_y}$
Upper arm	$\overline{u}\overline{a}_x = \overline{u}\overline{a}_y \times \overline{u}\overline{a}_z$	$\overline{u}\overline{a}_y = \frac{g\overline{h} - (\overline{m}_{el} + \overline{m}_{em})/2}{ g\overline{h} - (\overline{m}_{el} + \overline{m}_{em})/2 }$	$\overline{u}\overline{a}_z = \frac{\overline{m}_{us} - (\overline{m}_{el} + \overline{m}_{em})/2}{ \overline{m}_{us} - (\overline{m}_{el} + \overline{m}_{em})/2 \times \overline{u}\overline{a}_y}$
Forearm	$\overline{f}\overline{a}_x = \frac{\overline{m}_{us} - \overline{m}_{rs}}{ \overline{m}_{us} - \overline{m}_{rs} } \times \overline{f}\overline{a}_y$	$\overline{f}\overline{a}_y = \frac{(\overline{m}_{el} + \overline{m}_{em})/2 - \overline{m}_{us}}{(\overline{m}_{el} + \overline{m}_{em})/2 - \overline{m}_{us}}$	$\overline{f}\overline{a}_z = \overline{f}\overline{a}_x \times \overline{f}\overline{a}_y$
Hand	$\overline{h}_x = \frac{\overline{m}_{us} - \overline{m}_{rs}}{ \overline{m}_{us} - \overline{m}_{rs} } \times \overline{h}_y$	$\overline{h}_y = \frac{(\overline{m}_{rs} + \overline{m}_{us})/2 - \overline{m}_{m3}}{(\overline{m}_{rs} + \overline{m}_{us})/2 - \overline{m}_{m3}}$	$\overline{h}_z = \overline{h}_x \times \overline{h}_y$

influence was created to refine the mesh around the moving segments, where high velocity and pressure gradients are expected.

No velocity was imposed at the inlet, all gradients were null at the outlet, and the no-slip condition enforced at the body surface. The numerical flow simulation rests on the finite volume approach. The 3D incompressible, unsteady Navier–Stokes equations are discretized at the level of the body-conforming grid via the Fluent pressure-based segregated solver (Patankar, 1980), leading to the following system of nonlinear second-order partial differential (continuity and momentum) equations:

$$\nabla \cdot \mathbf{u} = 0, \tag{1}$$

and

$$\rho \left(\frac{\partial \mathbf{u}}{\partial t} + (\mathbf{u} \cdot \nabla) \mathbf{u} \right) = \rho \mathbf{g} - \nabla p + \mu \Delta \mathbf{u}, \tag{2}$$

where \mathbf{u} is the velocity vector, \mathbf{g} the body force per unit mass, p the pressure, and ρ and μ the density and dynamic viscosity of the fluid, respectively. The first-order implicit formulation was used for time discretization. No turbulence model was used in this study for the following reasons: (i) for a maximum stroke speed of 2.5 m s^{-1} and a characteristic arm–forearm length (the dimension along which the boundary layer develops) of either 0.08 m (thickness) or 0.10 m (width), this yielded a Reynolds number of 2.9×10^5 , indicative of a transitional flow; and (ii) for flow with massive separation at edges, the separation point location is theoretically insensitive to the Reynolds number (Hoerner, 1965)—numerically confirmed by Marinho et al. (2011) who found constant drag coefficient regardless of water flow speed—hence a very low effect of turbulences on hydrodynamic forces. For complex flow crossing the mesh lines obliquely, the second-order discretization was adopted to limit numerical diffusion. The PISO algorithm with skewness correction (uncoupled from neighbor correction) was used to deal with distorted meshes (ANSYS Fluent Release 14.5, Help System, ANSYS Fluent Theory Guide, ANSYS, Inc.). The convergence criterion was set at 10^{-3} .

2.3. Dynamic mesh algorithm

Most difficulties arise when numerically controlling joint deformation; the geometry is highly constrained. Joints must connect smoothly to the adjacent rigid surfaces to prevent negative cell volumes and the simulation to stop before completion. Triangle aspect ratios also require to be preserved for the solution to converge. These requirements must absolutely be respected to simulate full aquatic upper limb movements, and to compute the external forces necessary for inverse dynamics modeling. Yet, at present, no solutions are available in commercial CFD software. To achieve this, we built upon previous works in computer graphics (Kavan et al., 2008) and implemented a dual quaternion blending algorithm in C programming language within Fluent. Briefly, each 4×4 transformation matrix T_j that defines the instantaneous configuration of an upper limb joint j was computed and converted to its dual quaternion form $\hat{\mathbf{q}}_j$. These dual quaternions were linearly blended into a new, unit (normalized) dual quaternion $\hat{\mathbf{b}}' = \sum_{j=1}^n \frac{w_j \hat{\mathbf{q}}_j}{\|\sum_{j=1}^n w_j \hat{\mathbf{q}}_j\|}$ where n is 3, the number of upper limb joints; and w_j are the weights computed based on the distance from a vertex \mathbf{v} in neutral pose to its neighboring joints. The transformed vertex \mathbf{v}_c in the current pose then readily derived from the following relation: $\mathbf{v}_c = \hat{\mathbf{b}}' \mathbf{v} \hat{\mathbf{b}}'^*$, where $\hat{\mathbf{b}}'^*$ is the conjugate of $\hat{\mathbf{b}}'$. The resulting blended transformation does not contain shear or scale factors, which results in a smooth, skin-like animation free from skin-collapsing artifacts.

2.4. Inverse dynamics model

Since no existent interface readily links the external forces computed through CFD to the measurement of the joint load, we coded and implemented an inverse dynamics model of the upper limb through the homogeneous matrix approach, a compact notation derived from robotics that treats concomitantly linear and

rotational components (Legnani et al., 1996). There are sound reasons for the choice of this approach over the classical Newton–Euler vectorial equations: (i) the notation is convenient for computer applications; (ii) the method is poorly sensitive to kinematics measurement errors; (iii) importantly, no assumption about the type of joint being modeled is required, which makes the model suitable for complex joints (Doriot and Chèze, 2004).

Model inputs were the acceleration, pseudo-inertial, and action (drag, weight and buoyancy) matrices at every time step of the simulation. From the homogeneous transformation matrix $\mathbf{M}_{0,s}$ representing the attitude of the segment s with respect to the ICS, the acceleration matrix is obtained by:

$$\mathbf{H}_{s(0)} = \ddot{\mathbf{M}}_{0,s} \mathbf{M}_{0,s}^{-1}, \quad (3)$$

with $\ddot{\mathbf{M}}_{0,s}$ the second order derivative of the transformation matrix $\mathbf{M}_{0,s}$ and $\mathbf{M}_{0,s}^{-1}$ its inverse.

Segment masses m and center of mass positions \mathbf{r}_{COM} in the SCS were estimated from scaling equations based on subject anthropometry (Dumas et al., 2007), and used to build the inertial matrix $\mathbf{I}_{s(COM)}$. This matrix was displaced from the segment center of mass to the origin of the SCS according to the parallel axis theorem:

$$\mathbf{I}_{s(SCS)} = \mathbf{I}_{s(COM)} + m[(\mathbf{R} \cdot \mathbf{R})\mathbf{E}_3 - \mathbf{R} \otimes \mathbf{R}] = \begin{bmatrix} I_{xx} & I_{xy} & I_{xz} \\ I_{yx} & I_{yy} & I_{yz} \\ I_{zx} & I_{zy} & I_{zz} \end{bmatrix}, \quad (4)$$

where $\mathbf{I}_{s(SCS)}$ is the new inertia matrix, \mathbf{R} the displacement vector, and \mathbf{E}_3 the 3×3 identity matrix. The pseudo-inertial matrix \mathbf{J} of the segment s was finally derived as follows:

$$\mathbf{J}_{s(SCS)} = \begin{bmatrix} \frac{tr(\mathbf{I}_{s(SCS)})}{2} - I_{xx} & -I_{xy} & -I_{xz} & q_x \\ -I_{yx} & \frac{tr(\mathbf{I}_{s(SCS)})}{2} - I_{yy} & -I_{yz} & q_y \\ -I_{zx} & -I_{zy} & \frac{tr(\mathbf{I}_{s(SCS)})}{2} - I_{zz} & q_z \\ q_x & q_y & q_z & m \end{bmatrix}, \quad (5)$$

where $tr(\mathbf{I}_{s(SCS)})$ denotes the trace of the inertial matrix, and $\mathbf{q} = m\mathbf{r}_{COM}^T$ the product of the segment mass by the center of mass position.

Fluid forces and moments were calculated in the SCS from the action of the fluid on each face of the segment. Net fluid force \mathbf{f}_s on the segment s was computed as follows:

$$\mathbf{f}_s = \sum_{i=1}^n \mathbf{f}_i, \quad (6)$$

where \mathbf{f}_i is the sum of pressure and friction drag acting on the face i expressed in the SCS, and n the number of faces composing the segment surface. The resulting moment \mathbf{m}_s was given by:

$$\mathbf{m}_s = \sum_{i=1}^n \mathbf{r}_i \times \mathbf{f}_i, \quad (7)$$

where \mathbf{r}_i is the position vector of the centroid of face i in the SCS. Fluid forces and moments acting on the segment s were stored in the skew-symmetric action matrix $\phi_{F,s}$:

$$\phi_{F,s(SCS)} = \begin{bmatrix} 0 & -\mathbf{m}_z & \mathbf{m}_y & \mathbf{f}_x \\ \mathbf{m}_z & 0 & -\mathbf{m}_x & \mathbf{f}_y \\ -\mathbf{m}_y & \mathbf{m}_x & 0 & \mathbf{f}_z \\ -\mathbf{f}_x & -\mathbf{f}_y & -\mathbf{f}_z & 0 \end{bmatrix}, \quad (8)$$

Weight and buoyancy action matrices ($\phi_{W,s}$ and $\phi_{B,s}$) were evaluated in the ICS. Volume of upper limb segments and centers of buoyancy were determined from participants' upper limb scan models, which allowed for the computation of moments of buoyancy. Both action matrices were converted back in the SCS as follows:

$$\phi_{W,s(SCS)} = \mathbf{M}_{s,0} \phi_{W,s(0)} \mathbf{M}_{s,0}^{-1}, \quad (9)$$

$$\phi_{B,s(SCS)} = \mathbf{M}_{s,0} \phi_{B,s(0)} \mathbf{M}_{s,0}^{-1}. \quad (10)$$

Inverse dynamics calculations were then performed iteratively to solve for upper limb net joint forces and moments. The acceleration matrix $\mathbf{H}_{s(0)}$ was similarly converted in the SCS, and further multiplied by $\mathbf{J}_{s(SCS)}$ to yield the matrix \mathbf{A} containing the forces and moments producing the linear and angular acceleration of the segment s :

$$\mathbf{A}_{s(SCS)} = \mathbf{H}_{s(SCS)} \mathbf{J}_{s(SCS)} - \mathbf{J}_{s(SCS)} \mathbf{H}_{s(SCS)}^T. \quad (11)$$

The net forces and moments acting on a segment were stored in the following matrix:

$$\Phi_{s(SCS)} = \phi_{F,s(SCS)} + \phi_{W,s(SCS)} + \phi_{B,s(SCS)} + \mathbf{A}_{s(SCS)}, \quad (12)$$

and those acting at the proximal joint j of segment s were ultimately derived from:

$$\Phi_{j(SCS)} = \Phi_{s(SCS)} + \mathbf{M}_{s,s-1} \Phi_{j-1(SCS)} \mathbf{M}_{s,s-1}^{-1}, \quad (13)$$

with $\Phi_{j-1(SCS)}$, the action matrix describing net forces and moments at the joint $j-1$ distal to j in the distal SCS; $\mathbf{M}_{s,s-1}$, the transformation matrix of the distal SCS expressed in the proximal one; and $\mathbf{M}_{s,s-1}^{-1}$, its inverse.

To get a more coherent anatomical and clinical understanding of joint dynamics, joint forces and moments were described in non-orthogonal joint coordinate systems (JCS; (Schache and Baker, 2007; Wu et al., 2005)) according to formulas in Desroches et al. (2010) with the first axis (the above-mentioned Z) fixed in the proximal segment, the third axis (Y) fixed in the distal one, and the second (floating) axis defined as the cross product of the two others. Positive joint forces were compression, lateral and anterior shears; positive joint moments were flexion, adduction and internal rotation. Joint forces and moments were respectively normalized to body weight and body weight times arm length (Hof, 1996). To evaluate time series intra-individual variability (for each joint and about each axis), the mean deviation was computed across the four strokes of a single participant (Hanlon et al., 2012).

2.5. Preliminary validation

In order to stay vertically still at the surface, the momentum imparted to the body should equate to zero over a stroke, hence a null net impulse. In other words, according to Eq. (14), the impulse delivered by the action of both arms should balance the impulse of the 34-N ballast and the net buoyancy (13.7 ± 3.5 N, measured via the extra load necessary to immerse the body just below the surface after maximal inspiration):

$$2 \int_0^t \mathbf{f}_y dt = \left(f_{BALLAST} + \underbrace{f_{WEIGHT} - f_{BUOYANCY}}_{net\ buoyancy} \right) \cdot t, \quad (14)$$

where the center term is the integral over a stroke period t of the external forces acting on the upper limb segments, of which solely the vertical components \mathbf{f}_y were retained, multiplied by two to account for both arms (assuming symmetry). This impulse supposedly capable of supporting the ballasted swimmer computed from CFD was compared to the right term in Eq. (14) to assess the validity of the present simulations.

3. Results

The first necessary step was to evaluate simulation validity. The net impulse applied to the body over a stroke was 16.7 ± 4.4 N s, while that produced by the arms and computed from the present numerical simulations was 16.4 ± 4.2 N s, resulting in a gap of $1.2 \pm 3.5\%$.

Wrist, elbow and shoulder reaction forces and moments time series are plotted in Figs. 3 and 4. On an stroke-by-stroke basis, they were identical in profile, with mean deviation scores across four strokes $< 0.06\%BW$ and $0.11\%BW \cdot AL$ for joint forces and moments, respectively. Joint load was within $5\%BW$, with notable exceptions for shear forces along the posterior direction at the elbow ($8.1 \pm 0.6\%BW$), and anterior ($7.1 \pm 2.1\%BW$) and lateral ($7.0 \pm 1.3\%BW$) directions at the shoulder. Moment curves displayed two local extrema, with peaks occurring about 30 and 70% of stroke duration at the elbow, and about 20 and 80% at the shoulder; peaks were largely indiscernible at the wrist. The greatest moments were observed at the shoulder joint, with extension ($6.0 \pm 0.6\%BW \cdot AL$), external rotation ($4.9 \pm 0.4\% BW \cdot AL$), and adduction ($4.1 \pm 1.5\%BW \cdot AL$) in a descending order of magnitude, whereas they were flexion ($3.6 \pm 0.5\%BW \cdot AL$), internal rotation ($3.1 \pm 0.4\%BW \cdot AL$) and adduction ($3.0 \pm 0.6\% BW \cdot AL$) at the elbow, and adduction ($0.7 \pm 0.1\%BW \cdot AL$), flexion ($0.5 \pm 0.1\%BW \cdot AL$) and external rotation ($0.06 \pm 0.01\%BW \cdot AL$) at the wrist.

4. Discussion

We presented the first thorough picture of 3D upper limb joint kinetics during underwater cyclical movements, taken from the integrated use of numerical fluid flow simulation and inverse dynamics modeling. The first featured a novel dynamic mesh algorithm capable to smoothly deform body geometries from

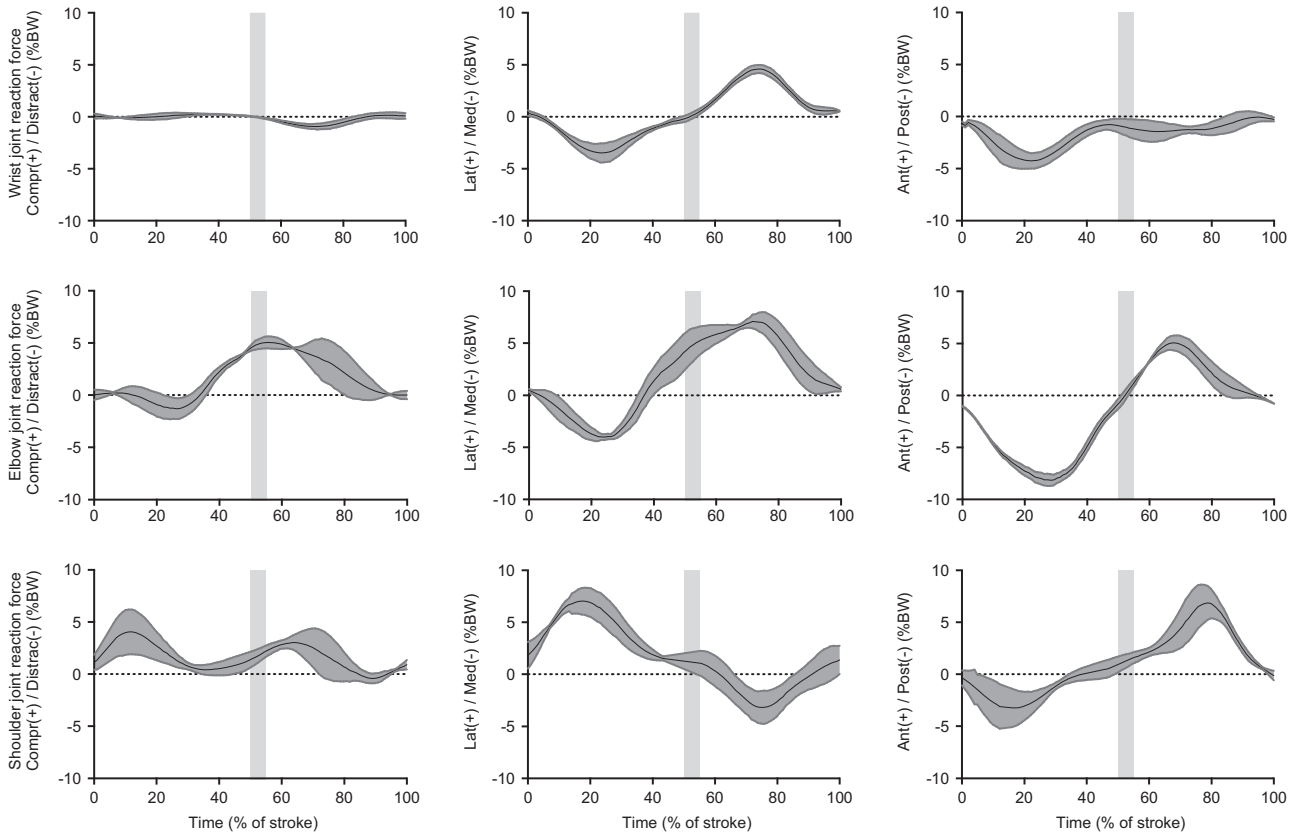


Fig. 3. Wrist, elbow and shoulder joint reaction (compression/distraction, lateral/medial and anterior/posterior shear) forces. The black solid line and dark gray area are group means and standard deviations ($N=28$ strokes), whereas the light vertical gray line represents the instant of stroke reversal; i.e., the transition between the downstroke and the upstroke.

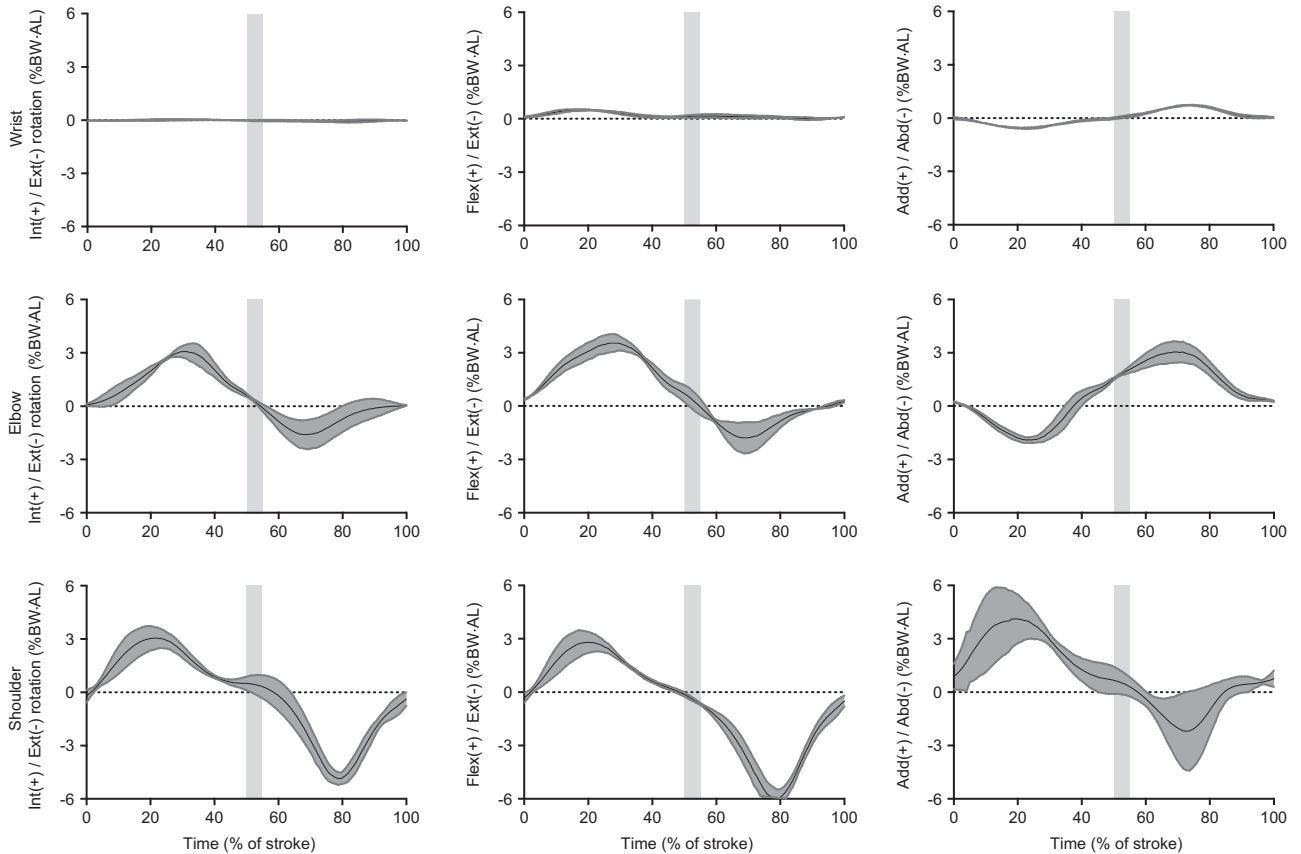


Fig. 4. Upper limb 3D joint moments about internal/external rotation, flexion/extension, and adduction/abduction axes. See Fig. 3 for color legend.

actual kinematics and compute instantaneous hydrodynamic forces at the upper limb in dynamic conditions. The latter was approached through the homogeneous matrix formulation, well adapted to Fluent programming language and suitable for modeling complex joints. The impulse calculated from the present simulations agreed (1.2% gap on average) with that theoretically determined from the impulse of net buoyancy and ballast forces, therefore validating our first hypothesis that this approach would be feasible and yield accurate results. In comparison to pressure sensors and strip theory approaches, our new methodology has the added benefits of providing a dual level of 3D kinetic evaluation, either at the surface of the segments through CFD or at the joint through inverse dynamics. Moreover, simulation spatial and temporal resolutions are respectively of the order of few millimeters and milliseconds, which lead to potent and ecological modeling, and discrimination of thin differences in morphology or kinematics, for example.

More practically, we predicted that upper limb joint load would be low enough to support the benefits of water on the body structure. Upper limb 3D joint forces were grossly within 5%BW, which is similar in magnitude to the joint load during walking in shallow water (Orselli and Duarte, 2011). On land, values of up to 35%BW were observed at the shoulder joint of disabled patients walking at $< 1 \text{ m s}^{-1}$ with crutches (Slavens et al., 2010), and approximately within 10%BW during manual wheelchair propulsion at 3 km h^{-1} (Gil-Agudo et al., 2010). Altogether, this supports the use of low-load upper limb aquatic exercises in males to prevent joint stress and confirms our second hypothesis. However, despite performing at low intensity, our approach highlights the fact that certain dimensions at certain joints (shoulder anterior and elbow lateral shears) might in some instances reach much higher stress of nearly 10%BW. These results question empirical rehabilitation protocols, and open the way to the scientific establishment of aquatic therapy.

Joint moments were similar in magnitude, revealing the balanced contribution of all muscle groups in this complex aquatic 3D motion. Surprisingly though, shoulder moments peaked earlier than at the elbow during the downstroke and vice versa during the upstroke, regardless of the axis of rotation. In other words, two loading patterns of the upper limb musculature were observed within the same movement. A proximo-distal sequencing of peak net joint moments has been identified since long as a fundamental motor control strategy of healthy biological systems to redistribute mechanical energy among segments and transmit power to the extremity (e.g., Marshall and Elliott, 2000; Putnam, 1993; Winters and Woo, 2012). Nonetheless, a disto-proximal organization is intriguing since it has never been discovered before at the upper limb. It may function as a strategy of stiffness regulation during on-land locomotion, essentially to provide a distal, compliant interface with the environment, and facilitate energy absorption by larger proximal muscles (Nichols et al., 2016). By analogy, perhaps aquatic environment instability is sensed distally at the hand and forearm, and the disto-proximal sequencing of peak net joint moments seen during the downstroke is a natural yet highly dynamic response to damp the perturbations.

The integrated use of CFD and inverse dynamics is a significant methodological improvement towards unique, fundamental insights into aquatic movement biomechanics. This is crucial to more applied forms of research on aquatic rehabilitation and other popular exercises in water (e.g., competitive swimming, fitness), for example, to document how to perform faster, or to provide clinicians with best practice guidelines. The present numerical simulations are based on real kinematics and body scans at very dense spatial and temporal resolutions, which make them suitable to explore differences between males and females in order to draw broader conclusions about joint load in

humans. Future works are directed towards the examination of joint power modulation and muscle function with emphasis on injury etiology and hydrotherapy implications.

Conflict of interest statement

The authors declare no conflict of interest.

Acknowledgements

The authors thank Gregory Lecrivain for early guidance in UDF writing and insightful discussions about dynamic mesh implementation.

References

- ANSYS Fluent Release 14.5, Help System, ANSYS Fluent Theory Guide, ANSYS, Inc, 2012.
- Biscarini, A., Cerulli, G., 2007. Modeling of the knee joint load in rehabilitative knee extension exercises under water. *J. Biomech.* 40, 345–355.
- Collins, S.H., Wiggan, M.B., Sawicki, G.S., 2015. Reducing the energy cost of human walking using an unpowered exoskeleton. *Nature* 522, 212–215.
- Costa, L., Mantha, V.R., Silva, A.J., Fernandes, R.J., Marinho, D.A., Vilas-Boas, J.P., Machado, L., Rouboa, A., 2015. Computational fluid dynamics vs. inverse dynamics methods to determine passive drag in two breaststroke glide positions. *J. Biomech.* 48, 2221–2226.
- Desroches, G., Chêze, L., Dumas, R., 2010. Expression of joint moment in the joint coordinate system. *J. Biomech. Eng.* 132, 114503.
- Doriot, N., Chêze, L., 2004. A three-dimensional kinematic and dynamic study of the lower limb during the stance phase of gait using an homogeneous matrix approach. *IEEE Trans. Biomed. Eng.* 51, 21–27.
- Dumas, R., Chêze, L., Verriest, J.-P., 2007. Adjustments to McConville et al. and Young et al. body segment inertial parameters. *J. Biomech.* 40, 543–553.
- Farris, D.J., Sawicki, G.S., 2012. The mechanics and energetics of human walking and running: a joint level perspective. *J. R. Soc. Interface* 9, 110–118.
- Gil-Agudo, A., Del Ama-Espinosa, A., Pérez-Rizo, E., Pérez-Nombela, S., Pablo Rodríguez-Rodríguez, L., 2010. Upper limb joint kinetics during manual wheelchair propulsion in patients with different levels of spinal cord injury. *J. Biomech.* 43, 2508–2515.
- Hanlon, M., Kearney, P., Condell, J., 2012. Kinematic variability in running: a caution regarding use of the spanning set measure. *J. Appl. Biomech.* 28, 99–104.
- Hansen, A.H., Childress, D.S., Miff, S.C., Gard, S.A., Mesplay, K.P., 2004. The human ankle during walking: implications for design of biomimetic ankle prostheses. *J. Biomech.* 37, 1467–1474.
- Hatze, H., 2002. The fundamental problem of myoskeletal inverse dynamics and its implications. *J. Biomech.* 35, 109–115.
- Heiderscheit, B.C., Chumanov, E.S., Michalski, M.P., Wille, C.M., Ryan, M.B., 2011. Effects of step rate manipulation on joint mechanics during running. *Med. Sci. Sport. Exerc.* 43, 296–302.
- Hoerner, S.F., 1965. *Fluid-dynamic Drag*, 2nd ed. Published by the author, Midland Park, NJ.
- Hof, A.L., 1996. Scaling gait data to body size. *Gait Posture* 4, 222–223.
- Kavan, L., Collins, S., Zára, J., O'Sullivan, C., 2008. Geometric skinning with approximate dual quaternion blending. *ACM Trans. Graph.* 27, 4, Article 105, 23 pages.
- Kudo, S., Yanai, T., Wilson, B., Takagi, H., Vennell, R., 2008. Prediction of fluid forces acting on a hand model in unsteady flow conditions. *J. Biomech.* 41, 1131–1136.
- Legnani, G., Casolo, F., Righettini, P., Zappa, B., 1996. A homogeneous matrix approach to 3D kinematics and dynamics – I. *Theory. Mech. Mach. Theory* 31, 573–587.
- Marinho, D.A., Silva, A.J., Reis, V.M., Barbosa, T.M., Vilas-Boas, J.P., Alves, F.B., Machado, L., Rouboa, A.I., 2011. Three-dimensional CFD analysis of the hand and forearm in swimming. *J. Appl. Biomech.* 27, 74–80.
- Marshall, R.N., Elliott, B.C., 2000. Long-axis rotation: the missing link in proximal-to-distal segmental sequencing. *J. Sport. Sci.* 18, 247–254.
- Nichols, T.R., Bunderson, N., Lyle, M., 2016. Neural regulation of limb mechanics: insights from the organization of proprioceptive circuits. In: Prilutsky, B.I., Edwards Jr, D.H. (Eds.), *Neuromechanical modeling of posture and locomotion*. Springer-Verlag, New York, NY, pp. 69–102.
- Orselli, M.I.V., Duarte, M., 2011. Joint forces and torques when walking in shallow water. *J. Biomech.* 44, 1170–1175.
- Patankar, S., 1980. *Numerical Heat Transfer and Fluid Flow*. Hemisphere, Washington, D.C.
- Putnam, C.A., 1993. Sequential motions of body segments in striking and throwing skills: descriptions and explanations. *J. Biomech.* 26 (Suppl 1), 125–135.
- Reed, M., Manary, M.A., Schneider, L.W., 1999. Methods for measuring and representing automobile occupant posture (No. 1999-01-0959). SAE Technical Paper.

- Roberts, T.J., Belliveau, R.A., 2005. Sources of mechanical power for uphill running in humans. *J. Exp. Biol.* 208, 1963–1970.
- Rouboa, A.I., Silva, A.J., Leal, L., Rocha, J., Alves, F.B., 2006. The effect of swimmer's hand/forearm acceleration on propulsive forces generation using computational fluid dynamics. *J. Biomech.* 39, 1239–1248.
- Sawicki, G.S., Ferris, D.P., 2008. Mechanics and energetics of level walking with powered ankle exoskeletons. *J. Exp. Biol.* 211, 1402–1413.
- Sawicki, G.S., Ferris, D.P., 2009. Mechanics and energetics of incline walking with robotic ankle exoskeletons. *J. Exp. Biol.* 212, 32–41.
- Schache, A.G., Baker, R., 2007. On the expression of joint moments during gait. *Gait Posture* 25, 440–452.
- Slavens, B.A., Sturm, P.F., Harris, G.F., 2010. Upper extremity inverse dynamics model for crutch-assisted gait assessment. *J. Biomech.* 43, 2026–2031.
- Takagi, H., Nakashima, M., Ozaki, T., Matsuuchi, K., 2013. Unsteady hydrodynamic forces acting on a robotic hand and its flow field. *J. Biomech.* 46, 1825–1832.
- Takagi, H., Shimada, S., Miwa, T., Kudo, S., Sanders, R., Matsuuchi, K., 2014. Unsteady hydrodynamic forces acting on a hand and its flow field during sculling motion. *Human. Mov. Sci.* 38, 133–142.
- Winter, D.A., 1983. Energy generation and absorption at the ankle and knee during fast, natural, and slow cadences. *Clin. Orthop. Relat. Res.*, 147–154.
- Winters, J.M., Woo, S.L.-Y., 2012. *Multiple Muscle Systems*. Springer-Verlag, New York, NY.
- Wu, G., van der Helm, F.C.T., Veeger, H.E.J.D., Makhsoos, M., Van Roy, P., Anglin, C., Nagels, J., Karduna, A.R., McQuade, K.J., Wang, X., Werner, F.W., Buchholz, B., Biomechanics, I.S.O., 2005. ISB recommendation on definitions of joint coordinate systems of various joints for the reporting of human joint motion—Part II: shoulder, elbow, wrist and hand. *J. Biomech.* 38, 981–992.
- Zaïdi, H., Taïar, R., Fohanno, S., Polidori, G., 2008. Analysis of the effect of swimmer's head position on swimming performance using computational fluid dynamics. *J. Biomech.* 41, 1350–1358.